First Principles Modeling of Nanostructures

Serdar ÖĞÜT
Dept. of Physics, University of Illinois at Chicago,
Chicago, IL 60607, USA

Abstract

Among the various theoretical tools for investigating microscopic material properties, *ab initio* (first principles) methods based on density functional theory and pseudopotentials have had a very good track record over the last two decades in terms of accuracy, reliability, and efficiency. The application of these methods to nanostructures to investigate their structural, electronic, and optical properties has, however, not been quite straightforward due to the large computational demand and new physics inherent in the nanometer and sub-nanometer size region. One particularly useful extension to overcome the computational demand imposed by localized nanostructures has been the introduction of methods based on a real-space implementation, such as the higher order finite difference pseudopotential method. In this review, first the basic theoretical tools of density functional theory, *ab initio* pseudopotentials, and higher-order finite difference method are briefly reviewed. Next, applications of the real-space higher-order finite difference *ab initio* pseudopotential method to different properties of various nanostructured materials are presented. These applications include (i) structural and electronic properties of small semiconductor (Si, Ge, GeTe) clusters, (ii) calculation of quasiparticle and exciton binding energies in Si quantum dots containing up to 1,000 atoms, and (iii) a new efficient real-space approach for calculating the microscopic dielectric screening matrix, its inverse, and the resulting exciton Coulomb energies in hydrogenated Si clusters up to ~ 1 nm diameter in size.

Key Words: First principles, pseudopotentials, density functional theory, real-space methods, nanostructures, semiconductor clusters, Si quantum dots, dielectric screening

1. Introduction

Computational materials science (CMS) is an interdisciplinary research area of physics, chemistry, and scientific computing [1]. Generally speaking, CMS can be thought of describing efforts in achieving a microscopic understanding of the interrelationships between composition, structure, and various materials properties through classical and quantum mechanical modeling. There are various aspects in trying to achieve this general goal. For example, prediction of electronic, structural, and dynamical properties of real materials through all sizes regimes (from atoms to clusters to bulk materials) in various phases (gas, liquid, and solid) and physical environments forms an important aspect of CMS. In order to understand properties of real materials, researchers sometimes have to perform computational experiments on hypothetical materials, and this approach, which is not readily accessible in laboratory experiments, may prove to be quite useful in microscopic elucidation of material properties. Another aspect and goal of studies in CMS is to assist in the prediction of new materials with technologically useful applications. Finally, development of new and efficient algorithms and analytical methods for investigating properties of simple and complex materials forms an equally important research focus area in CMS.

With respect to theoretical tools of CMS, one can broadly divide them into two groups; empirical and *ab initio* (first principles) methods. In empirical methods, one employs classical (such as pair potentials)

or quantum mechanical modeling (such as tight-binding) using various functional forms with adjustable parameters fitted to experimental observations or accurate calculations. Calculations based on empirical methods are generally quite fast from a computational point of view, but they may often lack the degree of accuracy and reliability needed to examine individual microscopic material properties. In *ab initio* methods, on the other hand, one uses quantum mechanical modeling with no adjustable parameters and few well-justified and tested approximations, and the atomic numbers of the constituent atoms are the only input to the calculations. These methods offer a level of accuracy one needs to understand most physical properties in a wide range of materials. However, compared to empirical methods, the high degree of accuracy and reliability of *ab initio* calculations is compensated by the large computational demand that they impose. One important class of such methods that have been very extensively used in the last two decades are the *ab initio* density functional methods.

1.1. Density Functional Theory

Density functional theory (DFT) provides a tractable way of solving the quantum equations of motions for a system of interacting electrons under an external potential, such as the electron-ion interaction potential v_{ion} in a solid. In 1964, Hohenberg and Kohn proved a famous theorem, which states that the ground state energy of an electron gas with a nondegenerate ground state under an external potential is a unique functional of the electron charge density $\rho(\mathbf{r})$ and that this energy functional assumes its minimum value (ground state energy) for the correct (ground state) $\rho(\mathbf{r})$ [2]. A year later, Kohn and Sham [3] expressed this charge density in terms of orthonormal single particle wavefunctions $\{\psi_n(\mathbf{r})\}$ as

$$\rho(\mathbf{r}) = \sum_{n,\text{occ.}} |\psi_n(\mathbf{r})|^2 \tag{1}$$

where the sum is over occupied single particle orbitals. This allowed them to write the ground state energy of the electron gas as

$$E[\rho(\mathbf{r})] = -\frac{1}{2}\sum_n \int \psi_n^\star(\mathbf{r})\nabla^2\psi_n(\mathbf{r}) + \int \rho(\mathbf{r})v_{\text{ion}}(\mathbf{r})d\mathbf{r} + \frac{1}{2}\iint \frac{\rho(\mathbf{r})\rho(\mathbf{r}')}{|\mathbf{r}-\mathbf{r}'|}d\mathbf{r}d\mathbf{r}' + E_{\text{xc}}[\rho(\mathbf{r})] \tag{2}$$

In this expression, the first term is the kinetic energy of a non-interacting electron gas at the same density, the second term is the potential energy due to the electron-ion interaction. The third term is the classical Hartree energy, and the last term is the so-called exchange-correlation energy. Treating $\psi_n(\mathbf{r})$ and $\psi_n^\star$ as the variational parameters, one arrives at a single particle Schrödinger equation,

$$\left(-\frac{1}{2}\nabla^2 + v_{\text{eff}}[\mathbf{r},\rho(\mathbf{r})]\right)\psi_n(\mathbf{r}) = \epsilon_n\psi_n(\mathbf{r}) \tag{3}$$

where the effective potential $v_{\text{eff}}[\mathbf{r},\rho(\mathbf{r})]$ is given as

$$v_{\text{eff}}[\mathbf{r},\rho(\mathbf{r})] = v_{\text{ion}}(\mathbf{r}) + \int \frac{\rho(\mathbf{r}')}{|\mathbf{r}-\mathbf{r}'|}d\mathbf{r} + v_{\text{xc}}[\rho(\mathbf{r})] \tag{4}$$

where $v_{\text{xc}}[\rho(\mathbf{r})] = \frac{\delta E_{\text{xc}}}{\delta\rho(\mathbf{r})}$ is the exchange-correlation potential. Due to the dependence of v_{eff} on $\rho(\mathbf{r})$, which depends on the solutions $\psi_n(\mathbf{r})$ of the Schrödinger equation, equations (1), (3), and (4), known as the Kohn-Sham (KS) equations, have to be solved self-consistently.

In actual implementation of DFT for investigating material properties, there is a large number of different approaches with respect to algorithms, basis functions, representation of the electron-ion interaction, computational space, and approximation to the exchange-correlation potential. Of all the different DFT methods, the *ab initio* pseudopotential total energy method is perhaps the most widely used state-of-the-art "method of choice" [4]. This method, which can be implemented in both momentum and real space, has a very good track record for investigating structural, electronic, and optical properties of a large variety of materials. In fact, an examination of major breakthroughs in *ab initio* materials modeling over the last two decades shows that pseudopotentials have played an invaluable role in this respect.

1.2. *Ab Initio* Pseudopotentials

The pseudopotential method relies on the separation (in both energy and space) of electrons into core and valence electrons and that most physical and chemical properties of materials are determined by valence electrons in the interstitial region. One can therefore combine the full ionic potential with that of the core electrons' to give an effective potential (called the pseudopotential), which acts on the valence electrons only. On top of this, one can also remove the rapid oscillations of the valence wavefunctions inside the core region such that the resulting wavefunction and potential are smooth. Figure 1 shows a schematic representation of a pseudopotential and a pseudowavefunction along with the corresponding all-electron counterparts. Beyond a chosen cutoff radius r_c, the all-electron and pseudofunctions (potential and wavefunction) are identical, while inside the core region both the pseudopotential and pseudowavefunction are smoothly varying. After the construction of these pseudofunctions for a single atom and ensuring that their scattering properties are almost identical to those of the all-electron functions, they can be used in any chemical environment without any significant loss of transferability [5].
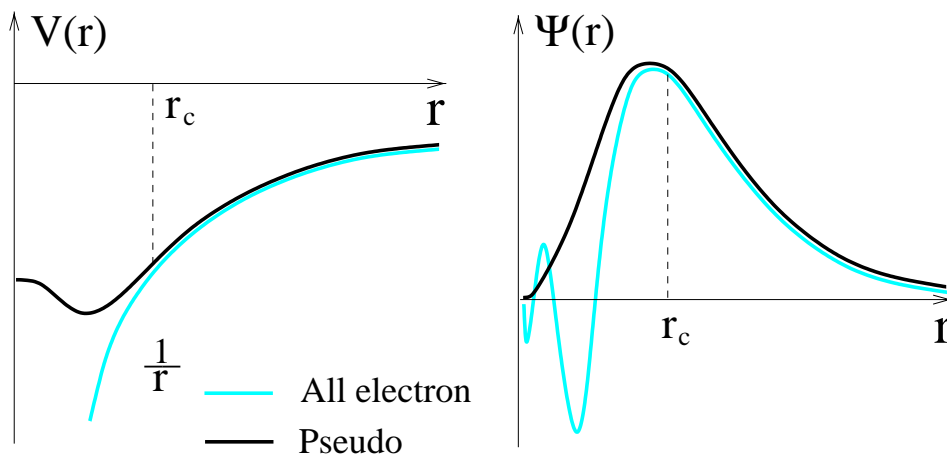
Figure 1. Schematic representation of a pseudopotential (left, dark curve) and a pseudowavefunction (right, dark curve) along with the all-electron potential (with the $1/r$ tail) and wavefunction (light curves). Notice that the all-electron and pseudofunctions are identical beyond the radial cutoff r_c and the pseudofunctions are smooth inside the core region.

There are various advantages of the pseudopotential method. By eliminating the core electrons from the problem, the number of particles for which the KS equations have to solved is decreased. For example, a pseudopotential calculation for bulk silicon (with 10 core and 4 valence electrons) requires the calculation of 4 occupied bands at each k-point, while an all-electron approach would require the calculation of 14 occupied bands. More importantly, the smooth spatial variation of the pseudopotential and pseudowavefunction allows the use of computationally convenient and unbiased basis, such as plane wave basis sets or grids in space.

1.3. Real Space Methods

The traditional approach to obtaining the electronic structure of a periodic solid with *ab initio* pseudopotentials has been to solve the KS equations in momentum space using a plane wave basis set [6]. There are many advantages of plane wave basis sets. For example, due to their completeness and orthonormality, they allow convenient and unbiased representation of the charge density and wavefunctions for calculating operator matrix elements. In addition, when plane waves are used with iterative diagonalization methods like Car-Parrinello [7] and conjugate gradient methods [4] there is a tremendous gain in efficiency in calculating self-consistent charge densities of large systems. For non-periodic and localized systems, such as defects, surfaces, clusters, quantum dots, using a plane wave basis set requires an artificial periodicity in order to implement standard electronic structure algorithms. This artificial periodicity is introduced through the use

of large unit cells called supercells. In a supercell calculation for a cluster, for example, the cluster is placed in a supercell large enough so that the electronic wavefunctions almost vanish near the supercell boundaries. This makes it possible to minimize the cell-cell interaction (with negligible dispersion of the molecular orbitals) while enabling the use of a plane wave basis to describe an isolated cluster via an "artificially periodic array" of clusters.

While the supercell approach works well for localized systems, typically a very large supercell is needed, which results in the plane wave basis replicating not only the relevant electronic states, but also "vacuum" regions imposed by the supercell. A much more efficient method to implement for investigating the electronic structures of localized systems is to solve the KS equations entirely on a real space grid using various methods [8, 9] such as the higher-order finite difference method. In the simplest and computationally convenient approach for a real-space method, one imposes a three-dimensional Cartesian grid of uniform spacing h. The system of interest (cluster, quantum dot, defect) is placed in a sphere of radius R, large enough so that the wavefunctions vanish outside of this sphere. The KS equations are solved on the discrete grid points labeled (x_i, y_j, z_k). A key aspect of the calculations in this method is related to the availability of higher-order finite difference expansions for the Laplacian ∇^2, which appears in the kinetic energy term of the KS equation. One can express the second order derivative of the wavefunction with respect to $x-$coordinate as

$$\frac{\partial^2 \psi}{\partial x^2} = \sum_{m=-M}^{m=M} C_m \psi(x_i + mh, y_j, z_k) + O(h^{2M+2}). \tag{5}$$

This expression is accurate up to $O(h^{2M+2})$, and the expansion coefficients C_m are readily available in the literature up to any order [8]. Typically, $M = 6$ is more than enough to describe the second order derivative of a smooth pseudowavefunction. When Eq. (3) is cast into a matrix equation of size N (where N is the number of grid points), all the potential terms reside on the diagonal, and the only off-diagonal terms come from the expansion coefficients C_m, resulting in a very sparse matrix which can be solved via various iterative matrix diagonalization schemes. In addition, the Hartree potential in Eq. (4) can be cast into a linear set of equations as the solutions of the Poisson equation $\nabla^2 V_H = -4\pi\rho(\mathbf{r})$, where the boundary terms are determined from multipole expansion of the charge density.
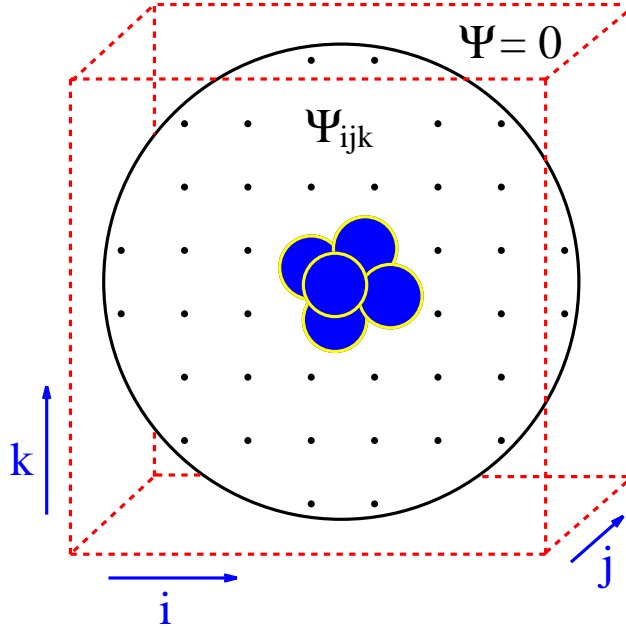
Figure 2. A schematic representation of a uniform Cartesian real-space grid for a cluster of atoms. The wavefunctions ψ_{ijk} are calculated on the grid points inside the sphere, and outside they are set to zero.

For localized systems, there are many important advantages of real space methods in comparison to the plane wave supercell approach. First, the method results in real symmetric sparse matrices (sparsity determined by the order M of the finite difference expansion), which makes it possible to use various efficient diagonalization schemes to solve the eigenvalue problem [10]. Second, since all the calculations are performed in real space, there is no need for fast Fourier transform resulting in easy parallelizability of the algorithms through a domain decomposition approach where each processor is responsible for a small portion of the physical domain [11]. Third, since the system is not repeated periodically, charged systems can be dealt with in a straightforward fashion by adding and subtracting the relevant charge without the use of a neutralizing background charge needed to avoid the divergence of Coulomb energy in a supercell approach.

Over the last 7 years, we have applied our *ab initio* pseudopotential higher-order finite difference method for investigations of structural, electronic, and optical properties of various semiconductor systems. For clusters and quantum dots of electronic materials such as Si, Ge, GaAs, GeTe, we investigated atomic structures, polarizabilities photoemission spectra, optical absorption, and dielectric screening [12, 13, 14, 15, 16, 17, 18, 19, 20]. In addition, we implemented a cluster approach for investigations of point defects such as vacancies, divacancies, impurities in Si and Ge [21, 22, 23]. These investigations have shed light on various microscopic properties of these nanostructures and their bulk defects. The rest of this paper will concentrate on some applications of the method to various semiconductor clusters, optical absorption in Si quantum dots, and a new formalism for calculating and storing inverse dielectric matrices of confined systems.

2. Semiconductor Clusters

A cluster is a finite assemblage of interacting atoms in a thermodynamically metastable state, i.e. clusters are stable only in isolation. Being an intermediate state between free atoms and bulk solids, atomic clusters, with their reduced dimensionality and large surface-to-volume ratio, have unique structural and electronic properties [24, 25]. The strong size dependence of these properties potentially makes it possible to fine-tune them for particular applications. As such, studies aimed at understanding the underlying physics and chemistry of clusters as a function of size are both fundamentally and technologically important. In trying to achieve this goal, one comes across many challenges. On the experimental side, for example, the lack of a direct probe of the atomic structure (such as X-ray diffraction and scanning tunneling microscopy for bulk materials) makes it necessary to use indirect methods like Raman spectroscopy or photoemission experiments. On the theoretical side, existence of open and unusual structures of semiconductor clusters (as opposed to their bulk form) requires the use of quantum (*ab initio*) forces, which is computationally more demanding compared to empirical approaches. In addition, numerous degrees of freedom and the existence of multiple local minima in the potential energy surfaces make structural optimization a very complex issue.

For systems with up to 10-20 atoms, the highly nontrivial issue of determining the minimum-energy structures of clusters from first principles can be handled using methods such as genetic algorithms [26] or simulated annealing. In particular, in our studies of various semiconductor clusters, we have used Langevin molecular dynamics (LMD) coupled to a simulated annealing procedure. In a typical LMD simulated annealing procedure, one starts the calculations at a high temperature (near 3000 K) from a random initial configuration of atoms, which are allowed to interact via quantum forces and with a fictitious heat bath and evolve according to the Langevin equation:

$$M_j \ddot{\mathbf{R}}_j = -\nabla_{\mathbf{R}_j} E\left(\{\mathbf{R}_j\}\right) - \gamma M_j \dot{\mathbf{R}}_j + \mathbf{G}_j \tag{6}$$

In this expression M_j and $\mathbf{R}_j$ denote the mass and position of the jth atom. The last two terms on the right hand side of Eq. (6) are the dissipation and fluctuation forces, respectively. The fluctuation forces are determined by random Gaussian variables $\{\mathbf{G}_i\}$ with a white noise spectrum,

$$\langle G_i^\alpha(t) \rangle = 0 \quad \text{and} \quad \langle G_i^\alpha(t) G_j^\alpha(t') \rangle = 2\gamma M_i k_B T \delta_{ij} \delta(t - t'). \tag{7}$$

The angular brackets denote ensemble or time averages, and α stands for the Cartesian component. The coefficient of temperature T ensures that the fluctuation-dissipation theorem is obeyed, i.e., the work done on the system is dissipated by the viscous medium. During the simulation, the system is cooled slowly, typically

in steps of 500 K, at each temperature the simulation running for $\sim$ 50-100 time steps. The stochastic nature of $\mathbf{G}_i$ helps the system escape from metastable states, sampling out reasonable low-energy structures, which are further refined at zero temperature.

Proceeding in this way, we have calculated the ground state structures of various semiconductor clusters such as Si_n, Ge_n (Fig. 3) and Ge_nTe_m (Fig. 4). The primary difference between Si and Ge clusters lies in the bondlengths, typically the bondlenghts of Ge clusters being a few percent larger than those of Si clusters. Also, the structures for group III-V semiconductor clusters (such as Ga_nAs_m) are observed to be similar to those of Si and Ge clusters [13]. As can be seen from these figures, these structures do not have much common with their bulk counterparts. Group IV-VI semiconductor clusters Ge_nTe_m are observed to generally adopt lower-symmetry structures compared to Si, Ge, and GaAs clusters [15]. At a given composition, the potential energy surfaces of Ge_nTe_m clusters possess local minima corresponding to higher-symmetry structures. The symmetry breaking for the global minimum is accompanied by a considerable gain in electronic energy and (usually) a widening of the energy gap, reminiscent of the Peierls distortion [27] observed in solid and liquid GeTe [28, 29, 30].
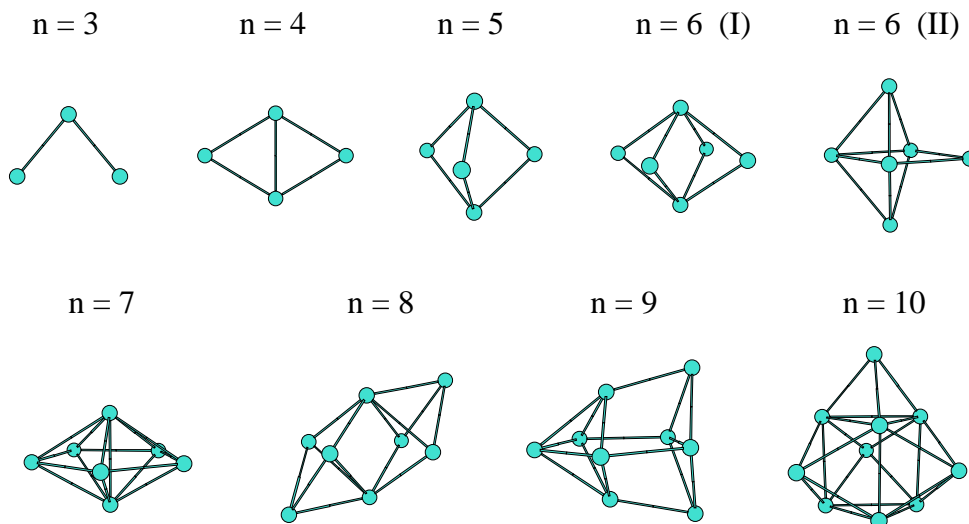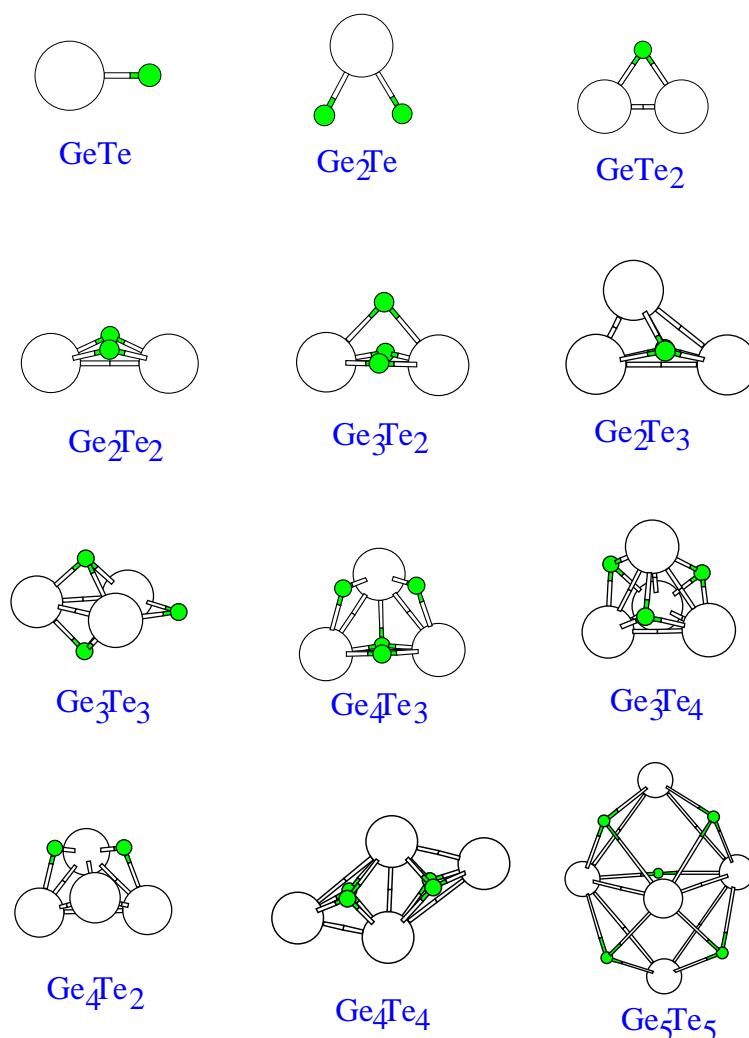

Figure 3. Minimum-energy structures of Si_n and Ge_n clusters. The two structures for $n = 6$ are energetically degenerate.
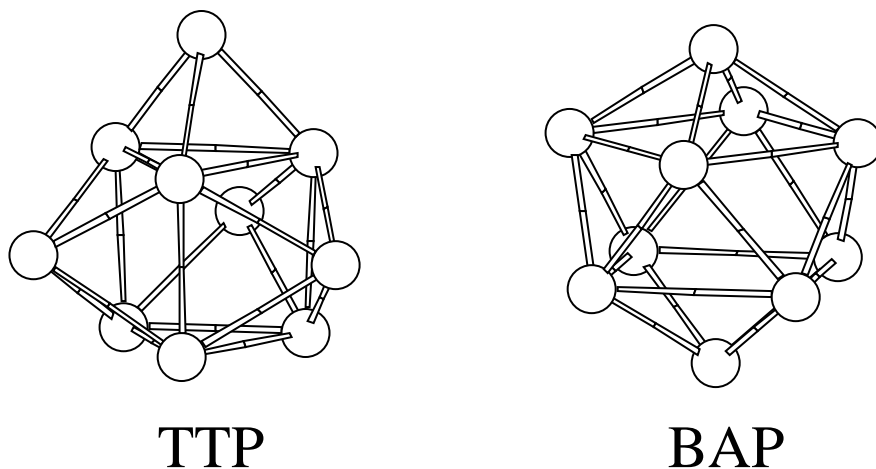
2.1. Photoemission Experiments

One of the earliest experiments performed to examine the electronic structures of small semiconductor clusters examined negatively charged Si_n and Ge_n ($n \leq 12$) clusters [31]. The photoemission spectra obtained in this work were used to gauge the energy gap between the highest occupied state and the lowest unoccupied state. While the first theoretical estimates for these gaps showed substantial disagreements with the measured values, later theoretical calculations emphasizing the importance of atomic relaxations upon charging brought a new perspective and very good agreement with experimental results [32]. In particular, it was observed that atomic relaxations as a result of charging might change dramatically the electronic spectra of certain clusters, and even reverse the relative stability of the energetically competing ground state structures of the neutral clusters [12].

The photoemission spectrum of Ge_{10}^- illustrates some of these key issues. Unlike Si_{10}^-, the experimental spectrum of Ge_{10}^- does not exhibit a gap. Cheshnovsky *et al.* interpreted this to mean that Ge_{10} does not

Figure 4. Minimum-energy structures of Ge_nTe_m clusters. Large empty balls represent Te atoms, while small filled balls represent Ge atoms.

exist in the same structure as Si_{10}, while our calculations find the same tetracapped trigonal prism (TTP) as the ground state structure of both Si_{10} and Ge_{10} (Fig. 5). The photoemission spectra for these clusters can be simulated by isothermal LMD, where the heat bath resembles a buffer gas in the experimental set-up. The simulated photoemission spectrum for Si_{10}^- is in very good agreement with the experimental results, reproducing both the threshold peak and other features in the spectrum. If a simulation is repeated for Ge_{10}^- using the TTP structure, the resulting photoemission spectrum is not in good agreement with experiment. However, there is no reason to believe that the TTP structure is correct for *negatively charged* Ge_{10}. In fact, we found that the bicapped antiprism (BAP) structure (Fig. 5) is slightly lower in energy for Ge_{10}^- compared to the TTP structure. The resulting spectra for both the TTP and BAP structures are shown in Fig. 6, and compared to the photoemission experiment. The calculated spectrum for the BAP structure is in very good agreement with the experimental result. Hence, while Si_{10} remains in the TTP structure in both its neutral and negatively charged state, charging reverses the relative stability of the TTP versus BAP structures in Ge_{10}, explaining the photoemission experiments. This observation suggests that interpretations of experimental results on charged clusters in terms of neutral cluster properties should be made cautiously by keeping in mind the possibility of substantial structural changes upon charging.

Figure 5. Tetracapped trigonal prism (TTP) and bicapped antiprism (BAP) structures of Ge_{10}.
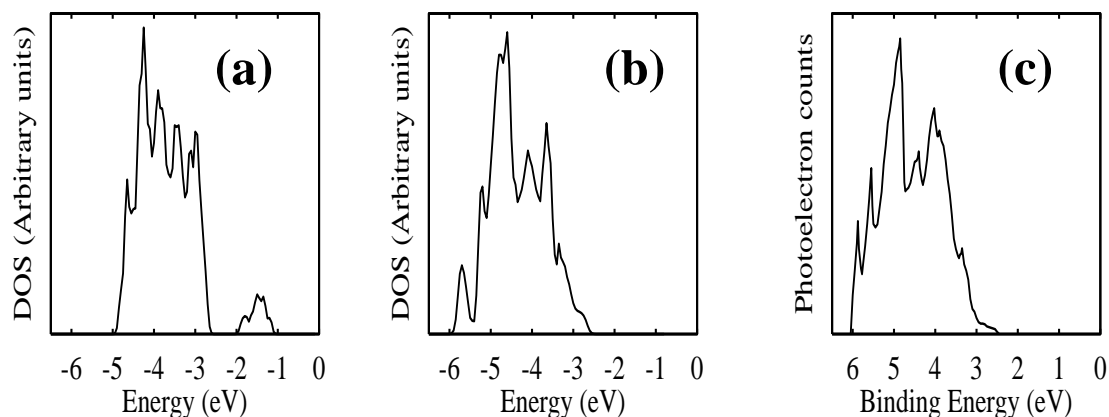
Figure 6. Calculated density of states for Ge_{10}^- with (a) the TTP structure; (b) the BAP structure. (c) shows the experimental photoemission spectrum of Ge_{10}^- (Ref. [31]).

3.   Optical Properties of Si Quantum Dots

Optical properties of semiconductor quantum structures with reduced dimensions have been the subject of many experimental and theoretical studies. One of the motivations for these studies has been stimulated by the discovery of visible luminescence from porous Si [33]. Over the last decade, this observation resulted in a great deal of interest in accurate calculations of excitation energies and quantum confinement (QC) effects in such important nanostructures as hydrogenated silicon clusters as well as other confined semiconductor quantum dots [16, 18, 34, 35, 36, 37, 38, 39, 40, 41, 42, 43]. Until 1997, almost all existing theoretical calculations on Si quantum dots were of semi-empirical nature. Such an approach postulates the transferability of bulk electronic interaction parameters to the nanocrystalline environment, the validity of which is not clear. More specifically, QC-induced changes in self-energy corrections, which may affect the magnitude of the optical gaps significantly, were neglected in semi-empirical calculations by implicitly assuming a "size-independent" correction which corresponds to that of the bulk. It naturally follows that a reliable way to investigate the optical gaps of quantum dots would be to perform *ab initio* calculations on these systems. However, there were two major bottlenecks for the application of first principles studies

450

to quantum dots. First, accurate *ab initio* calculations are limited, due to large computational demand, to small systems which usually do not correspond to the sizes of the nanoparticles for which experimental data are available. Second, even accurate *ab initio* calculations performed within the local density approximation (LDA) would suffer from the well-known underestimate of the band gap [44].

The first bottleneck, i.e. the large computational demand required in modeling quantum dots from first principles, can be overcome by straightforward application of new electronic structure algorithms, such as real space methods, to these confined systems using massively parallel computational platforms. As for the second problem, i.e. the underestimate of the band gap due to LDA, while sophisticated formalisms like the GW approximation [44] would be quite accurate, the confined nature of the quantum dots makes it possible for a simpler formulation of the fundamental quasiparticle gaps. For an n-electron system, the quasiparticle gap $\varepsilon_g^{\mathrm{qp}}$ can be expressed in terms of the ground state total energies E of the $(n+1)$-, $(n-1)$-, and n-electron systems as

$$\varepsilon_g^{\mathrm{qp}} = E(n+1) + E(n-1) - 2E(n) \tag{8}$$

$$= \varepsilon_g^{\mathrm{band}} + \Sigma, \tag{9}$$

where $\varepsilon_g^{\mathrm{band}}$ is the usual single-particle LDA band gap (defined as the eigenvalue difference between the lowest unoccupied and the highest occupied orbitals), and Σ is the self-energy correction.

The calculations for optical absorption in Si quantum dots were performed in real space using the higher-order finite difference pseudopotential method. Quantum dots were modeled by spherical bulk-terminated Si clusters that were passivated by hydrogen atoms at the boundaries (Fig. 7). We considered quantum dots up to 3 nm in diameter, the largest dot $Si_{705}H_{300}$ having more than 1000 atoms [16].
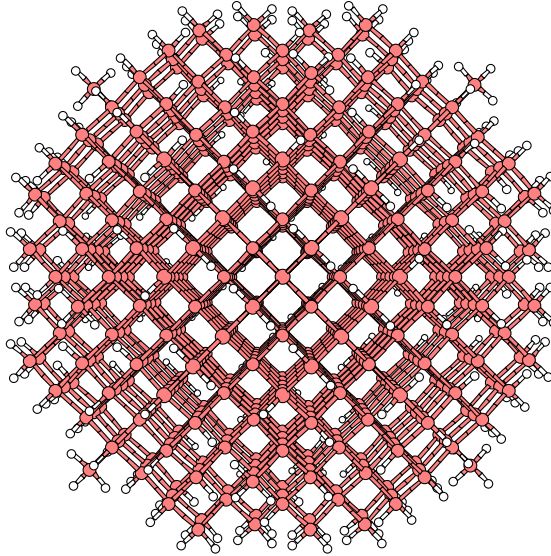
Figure 7. Atomic structure of $Si_{525}H_{276}$ quantum dot. The filled and empty circles represent the Si and H atoms, respectively. The diameter of this quantum dot is ≈ 2.7 nm.

Size dependences of the quasiparticle gap and self-energy correction are shown in Fig. 8. Both the gap values and self-energy corrections are enhanced substantially with respect to bulk values, and are inversely proportional to the dot diameter d as a result of QC. Specifically, $\varepsilon_g^{\mathrm{qp}}(d) - \varepsilon_{g,\mathrm{bulk}}^{\mathrm{qp}}$ and $\Sigma(d) - \Sigma_{\mathrm{bulk}}$ scale as $d^{-1.2}$ and $d^{-1.5}$, respectively. The quasiparticle gaps shown in Fig. 8 are significantly higher compared to the gap values obtained in earlier semi-empirical calculations [45, 46, 47, 48]. The main reason for this is the significant enhancement of electron self-energies due to QC, which cannot be properly taken into account in semi-empirical approaches. As shown in Fig. 8, even for a quantum dot with $d = 20$ Å, the self-energy correction is twice the bulk value of 0.68 eV.
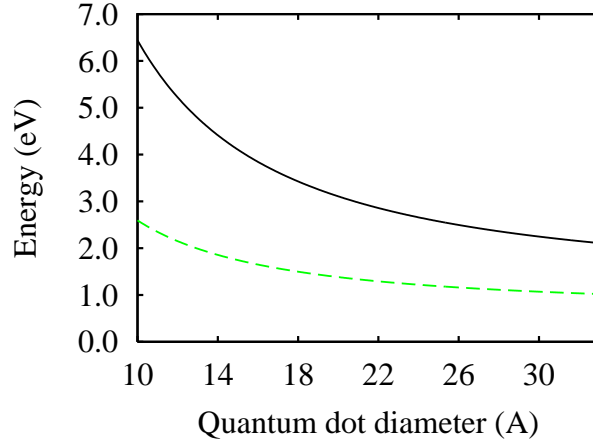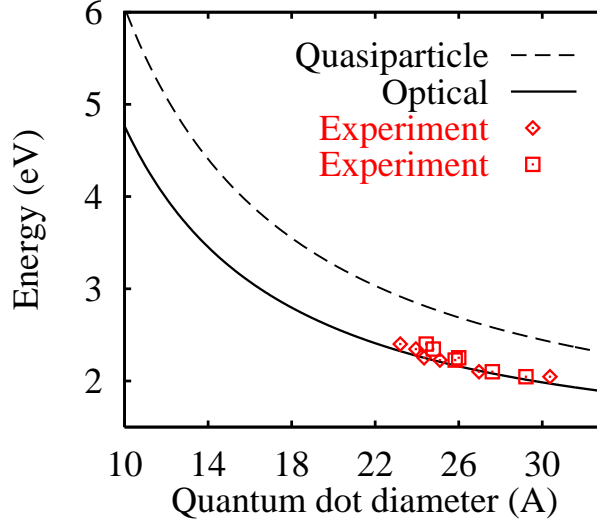
Figure 8. Calculated quasiparticle gaps (solid dark curve) and self-energy correction (light dashed curve) of Si quantum dots as a function of their diameter.

For direct comparison with experimental absorption data, exciton Coulomb and exchange energies need to be included. Compared to the Coulomb energy, exciton exchange energies are much smaller for the quantum dots studied here, and will therefore be neglected. QC in nanostructures enhances the bare exciton Coulomb interaction, and also reduces electronic screening, so that the exciton Coulomb energy E_{Coul} can be comparable to the quasiparticle gap. Therefore, in order to extract the optical gaps, this term needs to be included properly. An accurate calculation of E_{Coul} requires the microscopic calculation of dielectric response function $\epsilon(\mathbf{r}_1, \mathbf{r}_2)$. However, such a calculation for a quantum dot is quite cumbersome due to the large computational demand (see the next section). Using a model dielectric function based on the wavevector dependent dielectric functions of individual quantum dots [16], we calculated the screened exciton Coulomb energies in Si quantum dots. The resulting optical gaps $\varepsilon_g^{\mathrm{opt}} = \varepsilon_g^{\mathrm{qp}} - E_{\mathrm{Coul}}$ along with the quasiparticle gaps and experimental absorption data from Si nanocrystallites [49] are shown in Fig. 9. Although the calculated quasiparticle gaps are ~ 0.4 to 0.6 eV larger than the experimental absorption data, the calculated optical gaps are in excellent agreement with experiment. An interesting observation can be made about the good agreement of previous semi-empirical calculations with experiment [45, 47]. In the above semi-empirical approaches, it is the underestimate of *both* the quasiparticle gaps *and* the exciton Coulomb energies (through the use of a static dielectric constant of either the bulk or the quantum dot), that puts the calculated values in good agreement with experiment. As a matter of fact, the bare gaps of Refs. [45] and [47] without the exciton Coulomb energies are in better agreement with the experiment. These results demonstrate that (i) the quasiparticle gaps in Si quantum dots are actually higher than previously thought, and (ii) the exciton Coulomb energies, because of the wavevector dependence of the dielectric response function $\epsilon(\mathbf{r}_1, \mathbf{r}_2)$, are higher than previously calculated, resulting in optical gap values that are in good agreement with the experimental absorption data.

4.   *Ab Initio* Dielectric Screening in Si Nanocrystals

As discussed in the previous section, optical excitations in confined systems differ greatly from those in extended systems due to quantum confinement and surface effects; the increase in the 1.17 eV band gap of bulk Si to several volts in $\mathrm{Si}_n\mathrm{H}_m$ nanocrystals being an important example. The first step in the calculation of the optical gap usually involves the calculation of the quasiparticle gap, which is the energy needed to create a non-interacting electron-hole pair. The second component is due to the direct Coulomb (E_{Coul}) and exchange (E_{ex}) electron-hole interactions comprising the exciton binding energy. While this second term is quite negligible in bulk materials (~ 15 meV in crystalline Si), its value can increase by one to two orders of magnitude, hence become comparable to the quasiparticle gaps for nanoscale quantum structures

Figure 9. Calculated quasiparticle and optical gaps, and optical absorption data from Si:H microcrystallites taken from Ref. [49].

[37, 38, 42]. As a result, it is necessary to calculate exciton binding energies accurately in confined systems. An important part of such calculations involves obtaining the inverse screening dielectric matrix $\epsilon^{-1}(\mathbf{r}, \mathbf{r}')$.

The calculation of the full inverse screening dielectric matrix $\epsilon^{-1}(\mathbf{r}, \mathbf{r}')$ from first principles is computationally very demanding for confined systems. As a result, earlier approaches to estimating the exciton Coulomb energy in a Si quantum dot have used drastic approximations such as the static dielectric constant of either bulk Si [45, 47] or the quantum dot itself [43]. More recent studies have incorporated the spatial dependence of screening inside a quantum dot by using position-dependent model dielectric functions within generalized Penn [16] or Thomas-Fermi models [50], as well as a tight-binding approach [51]. The two main difficulties associated with *ab initio* calculations of the full $\epsilon^{-1}(\mathbf{r}, \mathbf{r}')$ arise in the inversion of ϵ and in calculations of such functions as $g(\mathbf{r}, \mathbf{r}'') = \int d\mathbf{r}' \epsilon^{-1}(\mathbf{r}, \mathbf{r}') f(\mathbf{r}', \mathbf{r}'')$. Both of these operations scale as N^3, where N is the number of grid points. Storing the entire ϵ or ϵ^{-1} matrix may not be possible due to memory requirement when N is large, as is the case for confined systems. Here, we present a new efficient method of obtaining and storing *ab initio* $\epsilon^{-1}(\mathbf{r}, \mathbf{r}')$ for confined systems, and use it to calculate perturbatively the exciton Coulomb energies in hydrogenated Si quantum dots as large as $Si_{35}H_{36}$ [20].

After obtaining the highest occupied molecular orbital (HOMO) and LUMO from the ground state calculation, the exciton Coulomb energy E_{Coul} can be written in a first-order perturbative formalism as

$$
\begin{aligned}
E_{\mathrm{Coul}} &= \int d\mathbf{r_1} |\psi_e(\mathbf{r_1})|^2 V_{\mathrm{scr}}^{\mathrm{h}}(\mathbf{r_1}) \\
&= \int d\mathbf{r_1} |\psi_e(\mathbf{r_1})|^2 \int d\mathbf{r} \epsilon^{-1}(\mathbf{r_1}, \mathbf{r}) V_{\mathrm{unscr}}^{\mathrm{h}}(\mathbf{r}) \\
&= \iiint \epsilon^{-1}(\mathbf{r_1}, \mathbf{r}) \frac{|\psi_e(\mathbf{r_1})|^2 |\psi_h(\mathbf{r_2})|^2}{|\mathbf{r} - \mathbf{r_2}|} d\mathbf{r} d\mathbf{r_1} d\mathbf{r_2}.
\end{aligned} \tag{10}
$$

In this expression, $V_{\mathrm{scr}}^{\mathrm{h}}$ and $V_{\mathrm{unscr}}^{\mathrm{h}}$ are screened and unscreened potentials due to the hole, ψ_e and ψ_h are the electron (LUMO) and hole (HOMO) wavefunctions, and ϵ^{-1} is the inverse of the static dielectric matrix. If we formally define $\tilde{\epsilon}^{-1}$ as

$$
\int \epsilon^{-1}(\mathbf{r_1}, \mathbf{r}) \frac{1}{|\mathbf{r} - \mathbf{r_2}|} d\mathbf{r} \equiv \tilde{\epsilon}^{-1}(\mathbf{r_1}, \mathbf{r_2}) \frac{1}{|\mathbf{r_1} - \mathbf{r_2}|}, \tag{11}
$$

then the exciton Coulomb energy can be written as

$$E_{\mathrm{Coul}} = \iint \tilde{\epsilon}^{-1}(\mathbf{r_1}, \mathbf{r_2}) \frac{|\psi_e(\mathbf{r_1})|^2 |\psi_h(\mathbf{r_2})|^2}{|\mathbf{r_1} - \mathbf{r_2}|} d\mathbf{r_1} d\mathbf{r_2}. \tag{12}$$

As a first step in computing E_{Coul} from Eq. (12), $\epsilon(\mathbf{r}, \mathbf{r}')$ needs to be calculated. Within density functional linear response theory, ϵ can be shown to have the following form [52]:

$$\epsilon(\mathbf{r}, \mathbf{r}') = \delta(\mathbf{r} - \mathbf{r}') - \int d\mathbf{r_1} \left[\frac{1}{|\mathbf{r} - \mathbf{r_1}|} + \frac{\delta^2 E_{\mathrm{xc}}}{\delta\rho(\mathbf{r})\delta\rho(\mathbf{r_1})} \right] \chi_0(\mathbf{r_1}, \mathbf{r}') \tag{13}$$

where E_{xc} is the exchange-correlation functional, and $\chi_0(\mathbf{r}, \mathbf{r}')$ is the independent particle polarizability:

$$\chi_0(\mathbf{r}, \mathbf{r}') = \sum_{i,j} (f_i - f_j) \frac{\psi_i^*(\mathbf{r})\psi_j(\mathbf{r})\psi_j^*(\mathbf{r}')\psi_i(\mathbf{r}')}{\varepsilon_i - \varepsilon_j} \tag{14}$$

as expressed in terms of the Kohn-Sham wavefunctions $\psi_i(\mathbf{r})$, the Kohn-Sham eigenvalues ε_i and occupation numbers f_i. With real wavefunctions and integer occupation numbers (as suitable for confined semiconductor systems), the expression for the static dielectric response function can be simplified by also taking spin-degeneracy into account as

$$\epsilon(\mathbf{r}, \mathbf{r}') = \delta(\mathbf{r} - \mathbf{r}') + 4 \sum_{v,c} (J_{vc}(\mathbf{r}) + K_{vc}(\mathbf{r})) \frac{\psi_v(\mathbf{r}')\psi_c(\mathbf{r}')}{\varepsilon_c - \varepsilon_v} \tag{15}$$

where the summations v, c are over the valence and conduction orbitals, and the integrals $J_{vc}(\mathbf{r})$ and $K_{vc}(\mathbf{r})$ are defined as

$$J_{vc}(\mathbf{r}) = \int d\mathbf{r_1} \frac{\psi_v(\mathbf{r_1})\psi_c(\mathbf{r_1})}{|\mathbf{r} - \mathbf{r_1}|} \tag{16}$$

$$K_{vc}(\mathbf{r}) = \int d\mathbf{r_1} \frac{\delta^2 E_{\mathrm{xc}}}{\delta\rho(\mathbf{r})\delta\rho(\mathbf{r_1})} \psi_v(\mathbf{r_1})\psi_c(\mathbf{r_1}) = \frac{\delta^2 E_{\mathrm{xc}}}{\delta\rho^2(\mathbf{r})} \psi_v(\mathbf{r})\psi_c(\mathbf{r}) \tag{17}$$

For calculating exciton Coulomb energies and many other physical quantities, the inverse of the $\epsilon(\mathbf{r}, \mathbf{r}')$ matrix is needed. As mentioned earlier, in terms of computational cost, this matrix inversion scales as N^3. In addition, the storage required by the full matrix naturally scales as N^2. Both the computational cost and the storage requirement become critical problems above $N \sim 10^4$. The form of the dielectric response function in Eq. (15) allows us to reduce this computational cost and storage requirement significantly by observing that $\epsilon(\mathbf{r}, \mathbf{r}')$ is separable in $\mathbf{r}$ and $\mathbf{r}'$. This makes it possible to express the matrix ϵ in terms of identity matrix I and rank $N_{vc} = N_v \times N_c$ matrices U and V, where N_v and N_c are the number of valence and conduction orbitals, respectively. The matrices U and V are defined as $U = 2(J_{vc} + K_{vc})$ and $V = 2\psi_v\psi_c/(\varepsilon_c - \varepsilon_v)$ for which the rows are labeled (from 1 to N) by grid points, and the columns are labeled (from 1 to N_{vc}) by valence and conduction orbital pairs. This leads to the following matrix expression for the response function,

$$\epsilon = I + UV^T, \tag{18}$$

where V^T is the transpose of matrix V. Expressing the ϵ matrix in this fashion allows us to calculate its inverse in terms of the inverse of the matrix $X = I + V^T U$ as follows:

$$\epsilon^{-1} = (I + UV^T)^{-1} = I - UX^{-1}V^T \tag{19}$$

We note that X is a $N_{vc} \times N_{vc}$ matrix, which implies that compared to direct inversion of the ϵ matrix, this method of finding ϵ^{-1} is faster by a factor of $(N/N_{vc})^3$, which can be as large as several orders of magnitude depending on the physical domain size ($N \propto R^3$), the grid spacing h ($N \propto h^{-3}$), and the number of occupied orbitals ($N_v \propto n_{\mathrm{atom}}$). In addition, the full $\epsilon(\mathbf{r}, \mathbf{r}')$ or $\epsilon^{-1}(\mathbf{r}, \mathbf{r}')$ no longer needs to be stored. Instead, two $N \times N_{vc} < N^2$ arrays (U and V) need to be saved. Another advantage of the separability of ϵ is in the calculation of functions $g(\mathbf{r}, \mathbf{r}'') = \int d\mathbf{r}' \epsilon^{-1}(\mathbf{r}, \mathbf{r}') f(\mathbf{r}', \mathbf{r}'')$. The calculation of the effective screening

function $\tilde{\epsilon}^{-1}(\mathbf{r_1}, \mathbf{r_2})$ in Eq. (11) is one example. Even if one were able to store the entire ϵ^{-1} matrix, the calculation of $\tilde{\epsilon}^{-1}$ would still be an N^3 operation. With the current expression in Eq. (19), this operation can be performed with two matrix-vector multiplications and scales as $N_{vc}N^2$. A striking example of the savings in computational time and memory can be given for the case of SiH$_4$. Due to convergence problems associated with the LUMO of this cluster, we used a domain size of $R = 20$ a.u, a grid spacing of $h = 0.5$ a.u, and $N_c = 26$ unoccupied states. This results in an ϵ matrix of dimension $N \sim 270,000$ and $N_{vc} = 104$. Storing the entire ϵ matrix would require ~ 600 GB of memory. Instead, the new method requires a modest 450 MB of memory, and is faster by a factor of ~ 3500. While this example is certainly an extreme case due to the special convergence problems in SiH$_4$, the computational savings for most confined systems will be quite significant, since N_{vc} will usually be considerably smaller than N [20].

The calculated exciton Coulomb and binding energies $E_b = E_{\text{Coul}} - E_{\text{ex}}$ for all clusters considered (SiH$_4$, Si$_2$H$_6$, Si$_5$H$_{12}$, Si$_{10}$H$_{16}$, Si$_{14}$H$_{20}$, Si$_{35}$H$_{36}$) are shown in Fig. 10, along with spin-triplet excitation values from Quantum Monte Carlo (QMC) and GW-Bethe-Salpeter (GW-BS) calculations [37, 38]. Also shown are the average effective dielectric constants $\overline{\epsilon}$ defined as the ratio of the unscreened Coulomb energy to the screened Coulomb energy [$\overline{\epsilon} = E_{\text{Coul}}(\epsilon = 1)/E_{\text{Coul}}$]. As expected, the unscreened Coulomb energies are quite large due to quantum confinement, ranging from about 5 eV in silane to 3.2 eV for a quantum dot of diameter 1.1 nm (Si$_{35}$H$_{36}$). Furthermore, we find that the screening in these quantum dots is very ineffective, as demonstrated by the large values of screened exciton Coulomb energies in Fig. 10. Although $\overline{\epsilon}$ increases steadily in going from SiH$_4$ to Si$_{35}$H$_{36}$ (as expected from quantum confinement models), the actual values of $\overline{\epsilon}$ (from 1.1 to 1.4) are very small compared with the bulk dielectric constant of 11.4. Comparison of the exciton Coulomb energies with binding energies E_b shows, as expected, that the attractive direct Coulomb interaction is at least one order of magnitude than the repulsive exchange interaction. Finally, the results obtained using the simple perturbative formalism of Eq. (10) agree very well with exciton binding energies for spin-triplet excitations calculated from the more sophisticated QMC and GW-BS formalisms.
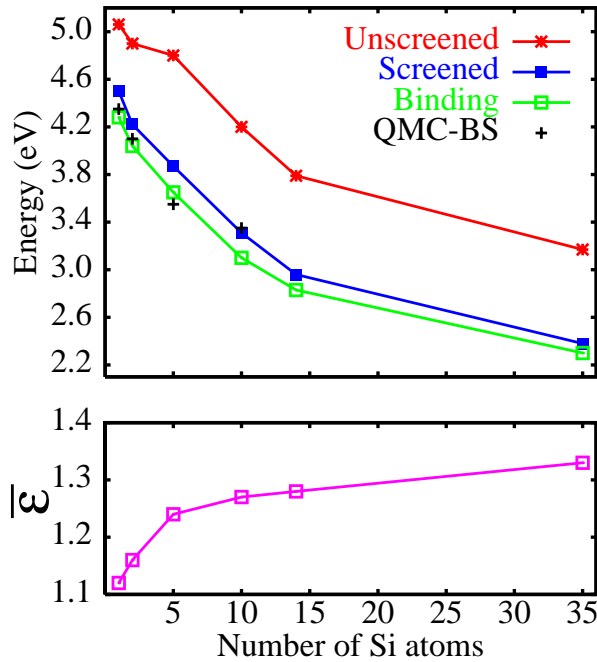
Figure 10. Calculated unscreened and screened exciton Coulomb energies, exciton binding energies, and average effective dielectric constants $\overline{\epsilon}$ (defined in the text) along with results from Quantum Monte Carlo (QMC) and Bethe-Salpeter (BS) calculations.

We also examined the spatial variation of the screening function $\tilde{\epsilon}^{-1}(\mathbf{r_1}, \mathbf{r_2})$ in order to address dielectric screening in quantum dots with better empirical models based on *ab initio* calculations. Clearly, a computa-

tionally convenient model dielectric function is one that depends only on the particle separation $r = |\mathbf{r_1} - \mathbf{r_2}|$. We therefore set $\mathbf{r_1} = \mathbf{0}$, and plotted $1/\tilde{\epsilon}^{-1}(\mathbf{0}, \mathbf{r_2})$ as a function of the distance from the origin. Since the actual $\tilde{\epsilon}$ is not spherically symmetric (only the symmetry-related positions have the same value), we averaged $\tilde{\epsilon}^{-1}(\mathbf{0}, \mathbf{r_2})$ over the positions $\mathbf{r_2}$ with $|\mathbf{r_2}| = r$. The resulting function $\overline{\epsilon}(r) = 1/\tilde{\epsilon}^{-1}(0, r)$ is plotted in Fig. 11
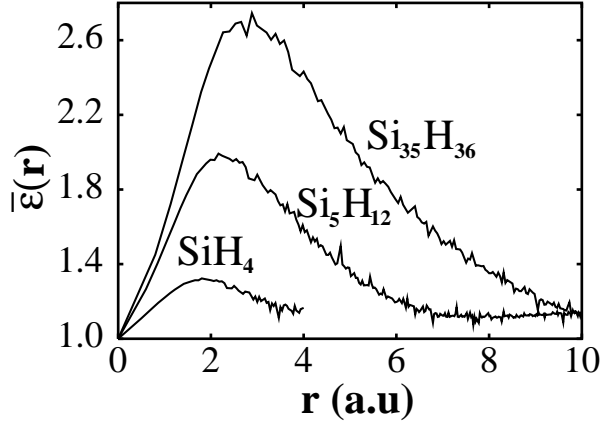
Figure 11. The averaged screening functions $\overline{\epsilon}(r) = 1/\tilde{\epsilon}^{-1}(0, r)$ for the three quantum dots SiH_4, Si_5H_{12}, and $Si_{35}H_{36}$. Their effective radii are 3.2 a.u., 5.4 a.u., and 10.4 a.u., respectively.

The effective screening functions $\overline{\epsilon}(r)$ are seen to increase rapidly and peak at a distance typically smaller than the effective radius of the quantum dot. After this peak, the screening function $\overline{\epsilon}(r)$ approaches unity, as it should, since the quantum dot is in vacuum. This type of behavior is substantially different from those predicted by empirical Thomas-Fermi model dielectric screening functions used in some earlier calculations. For example, the extension of Resta's model (developed for *bulk* semiconductors) [53] to quantum dots [50] results in an effective $\overline{\epsilon}(r)$ that becomes equal to the static dielectric constant of the quantum dots outside a radius R_∞. When such models are used in exciton Coulomb energy calculations, they predict much smaller exciton Coulomb energies than those calculated from *ab initio* screening dielectric matrices [54]. In addition, since these models treat the quantum dot as a homogeneous region outside of R_∞, it becomes necessary to take into account extra empirical terms due to surface polarization [50, 51, 55]. Our method, which makes it possible to obtain the full inverse dielectric matrix, avoids all these problems, and results in large exciton Coulomb energies due to ineffective screening inside the quantum dot and the presence of a surface.

Acknowledgements

References

[1] J. Bernholc, *Phys. Today*, **52**(9), (1999), 30.

[2] P. Hohenberg and W. Kohn, *Phys. Rev.*, **136**, (1964), B864.

[3] W. Kohn and L.J. Sham, *Phys. Rev.*, **140**, (1965), A1133.

[4] M.C. Payne, M.P. Teter, D.C. Allan, T. Arias, and J.D. Joannopoulos, *Rev. Mod. Phys.*, **64**, (1992), 1045.

[5] M.T. Yin and M.L. Cohen, *Phys. Rev. B*, **25**, (1982), 7403; G.B. Bachelet, D.R. Hamann, M. Schlüter, *ibid.*, **26**, (1982), 4199; A.M. Rappe, K.M. Rabe, E. Kaxiras, and J.D. Joannopoulos, *ibid.*, **41**, (1990), R1227; D. Vanderbilt, *ibid.*, **41**, (1990), R7892; N. Troullier and J. L. Martins, *ibid.*, **43**, (1991), 1993.

[6] J. Ihm, A. Zunger, and M.L. Cohen, *J. Phys. C*, **12**, (1979), 4409.

[7] R. Car and M. Parrinello, *Phys. Rev. Lett.*, **55**, (1985), 2471.

[8] J.R. Chelikowsky, N. Troullier, and Y. Saad, *Phys. Rev. Lett.*, **72**, (1994), 1240.

[9] E.L. Briggs, D.J. Sullivan, and J. Bernholc, *Phys. Rev. B*, **52**, (1995), R5471; F. Gygi and G. Galli, *ibid.*, **52**, (1995), R2229; G. Zumbach, N.A. Modine, and E. Kaxiras, *Solid State Commun.*, **99**, (1996), 57.

[10] Y. Saad, A. Stathopoulos, J.R. Chelikowsky, K. Wu, and S. Öğüt, *BIT*, **36**, (1996), 563.

[11] A. Stathopoulos, S. Öğüt, Y. Saad, J.R. Chelikowsky, and H. Kim, *Comput. Sci. Eng.*, **2**, (2000), 19.

[12] S. Öğüt and J.R. Chelikowsky, *Phys. Rev. B*, **55**, (1997), R4917.

[13] I. Vasiliev, S. Öğüt, and J.R. Chelikowsky, *Phys. Rev. Lett.*, **78**, (1997), 4805.

[14] I. Vasiliev, S. Öğüt, and J.R. Chelikowsky, *Phys. Rev. B*, **60**, (1999), R8477.

[15] R. Natarajan and S. Öğüt, *Phys. Rev. B*, **67**, (2003), 235325.

[16] S. Öğüt, J.R. Chelikowsky, and S.G. Louie, *Phys. Rev. Lett.*, **79**, (1997), 1770; *Proceedings of the 9th CIMTEC-World Forum on New Materials*, ed. P. Vincenzini and A. Eposti, (1999) pp. 3.

[17] I. Vasiliev, S. Öğüt, and J.R. Chelikowsky, *Phys. Rev. Lett.*, **82**, (1999), 1919.

[18] I. Vasiliev, S. Öğüt, and J.R. Chelikowsky, *Phys. Rev. Lett.*, **86**, (2001), 1813.

[19] I. Vasiliev, S. Öğüt, and J.R. Chelikowsky, *Phys. Rev. B*, **65**, (2002), 115416.

[20] S. Öğüt, R. Burdick, Y. Saad, and J.R. Chelikowsky, *Phys. Rev. Lett.*, **90**, (2003), 127401.

[21] S. Öğüt, H. Kim, and J.R. Chelikowsky, *Phys. Rev. B*, **56**, (1997), R11353.

[22] S. Öğüt and J.R. Chelikowsky, *Phys. Rev. Lett.*, **83**, (1999), 3852.

[23] S. Öğüt and J.R. Chelikowsky, *Phys. Rev. B*, **64**, (2001), 245206.

[24] M. Jarrold, *Science*, **252**, (1991), 1085.

[25] B. Hartke, *Angew. Chem. Int. Ed.*, **41**, (2002), 1468.

[26] D. Deaven and K. M. Ho, *Phys. Rev. Lett.*, **75** (1995), 288.

[27] R.E. Peierls, *Quantum Theory of Solids* (Oxford, Clarendon 1955), p. 108.

[28] P.B. Littlewood and V. Heine, *J. Phys. C: Solid State Phys.*, **12**, (1979), 4431.

[29] J.-P. Gaspard, A. Pellegatti, F. Marinelli, and C. Bichara, *Philos. Mag. B*, **77**, (1988), 727.

[30] J.Y. Raty, V. Godlevsky, P. Ghosez, C. Bichara, J.P. Gaspard, and J.R. Chelikowsky, *Phys. Rev. Lett.*, **85**, (2000), 1950; J.Y. Raty, V.V. Godlevsky, J.P. Gaspard, C. Bichara, M. Bionducci, R. Bellissent, R. Céolin, J.R. Chelikowsky, and Ph. Ghosez, *Phys. Rev. B*, **65**, (2002), 115205.

[31] O. Cheshnovsky, S.H. Yang, C. L. Pettiette, M.J. Craycraft, and R.E. Smalley, *Chem. Phys. Lett.*, **138**, (1987), 119.

[32] N. Binggeli and J.R. Chelikowsky, *Phys. Rev. Lett.*, **75**, (1995), 493.

[33] L.T. Canham, *Appl. Phys. Lett.*, **57**, (1990), 1046.

[34] A.D. Yoffe, *Adv. Phys.*, **50**, (2001), 1.

[35] A. Puzder, A.J. Williamson, J.C. Grossman, and G. Galli, *Phys. Rev. Lett.*, **88**, (2002), 097401.

[36] I. Vasiliev, J.R. Chelikowsky, and R.M. Martin, *Phys. Rev. B*, **65**, (2002), 121302.

[37] A.R. Porter, M.D. Towler, and R.J. Needs, *Phys. Rev. B*, **64**, (2001), 035320.

[38] J.C. Grossman, M. Rohlfing, L. Mitas, S.G. Louie, and M.L. Cohen, *Phys. Rev. Lett.*, **86**, (2001), 472.

[39] C.S. Garoufalis and A.D. Zdetsis, *Phys. Rev. Lett.*, **87**, (2001), 276402.

[40] C. Delerue, M. Lannoo, and G. Allan, *Phys. Rev. Lett.*, **84**, (2000), 2457.

[41] M.V. Wolkin, J. Jorne, P.M. Fauchet, G. Allan, and C. Delerue, *Phys. Rev. Lett.*, **82**, (1999), 197.

[42] M. Rohlfing and S.G. Louie, *Phys. Rev. Lett.*, **80**, (1998), 3320.

[43] A. Franceschetti and A. Zunger, *Phys. Rev. Lett.*, **78**, (1997), 915.

[44] M.S. Hybertsen and S.G. Louie, *Phys. Rev. B*, **34**, (1986), 5390.

[45] J.P. Proot, C. Delerue, and G. Allan, *Appl. Phys. Lett.*, **61**, (1992), 1948.

[46] T. Takagahara and K. Takeda, *Phys. Rev. B*, **46**, (1992), 15578.

[47] L.W. Wang and A. Zunger, *J. Phys. Chem.*, **98**, (1994), 2158.

[48] N.A. Hill and K.B. Whaley, *Phys. Rev. Lett.*, **75**, (1995), 1130; *ibid.*, **76** (1996) 3039.

[49] S. Furukawa and T. Miyasato, *Phys. Rev. B*, **38**, (1988), 5726.

[50] F.A. Reboredo, A. Franceschetti, and A. Zunger, *Phys. Rev. B*, **61**, (2000), 13073.

[51] C. Delerue, M. Lannoo, and G. Allan, *Phys. Rev. B*, **56**, (1997), 15306.

[52] M.S. Hybertsen and S.G. Louie, *Phys. Rev. B*, **35**, (1987), 5585.

[53] R. Resta, *Phys. Rev. B*, **16**, (1977), 2717.

[54] S. Öğüt and J.R. Chelikwosky (unpublished).

[55] S. Öğüt, J.R. Chelikwosky, and S.G. Louie, *Phys. Rev. Lett.*, **83**, (1999), 1270.